Output Regulation Control for Satellite Formation Flying Using Differential Drag

Shouman, Mohamed
Department of Aeronautics and Astronautics, Kyushu University : Doctoral Program

Bando, Mai
Department of Aeronautics and Astronautics, Kyushu University : Associate Professor

HOKAMOTO, Shinji
Department of Aeronautics and Astronautics, Kyushu University : Professor

出版情報：Journal of guidance, control, and dynamics. 42 (10), pp.2220-2232, 2019-07-25. American Institute of Aeronautics and Astronautics
バージョン：

Output Regulation Control for Satellite Formation Flying Using Differential Drag

Mohamed Shouman, [1] Mai Bando, [2] and Shinji Hokamoto [3]
Kyushu University, 744 Motoka, Nishi-ku, Fukuoka 819-0395, JAPAN

This paper proposes a new approach of using differentials in aerodynamic drag in combination with thrusters to control satellite formation flying in low Earth orbits. Parameterized output regulation theory for formation flying missions with combined control action is developed based on the Schweighart-Sedwick relative dynamics equations. The theory is implemented to precisely track the different trajectories of reference relative motion and eliminates the effects of the J_2 perturbations. The parametric Lyapunov algebraic equation is proposed to ensure the stability of the linear relative model subject to saturated inputs. The main goal of this study is to approve the viability of using the differentials in aerodynamic drag to precisely control different formation flying missions. Numerical simulations using a high fidelity relative dynamics model and a high-precision orbit propagator are implemented to validate and analyze the performance of the proposed control algorithm in comparison with the linear quadratic regulator algorithm based on actual satellite models.

I. Introduction

Satellite formation flying (SFF), a research area that forms part of spacecraft dynamics and control, has become an important field of research in recent years because it has several applications in Earth-observing missions. SFF can distribute the functionality of a single large satellite to multiple small satellites, thereby obviating the need for a complicated design. It also has attrac-

[1] Ph.D. Student, Department of Aeronautics and Astronautics/Mohamed.Shouman@aero.kyushu-u.ac.jp
[2] Associate Professor, Department of Aeronautics and Astronautics/mbando@aero.kyushu-u.ac.jp. Member AIAA.
[3] Professor, Department of Aeronautics and Astronautics/hokamoto@aero.kyushu-u.ac.jp. Member AIAA.

tive benefits such as offering a low-cost solution and adding flexibility to space-based programs by reducing the size and complexity of the spacecraft, which in turn enhances the reliability. SFF is also a key technology for missions that use interferometry, which, compared to using a single aperture, can achieve a higher resolution by combining images captured by several sensors.

A challenge that needs to be overcome when implementing SFF is to maintain the flying formation in the face of various perturbing factors. In this regard, the utilization of aerodynamic drag to generate control action has been suggested as a technology to maintain the formation in Low Earth Orbits (LEOs). An example of the practical mission is JC2Sat, which had been planned to be a joint mission of JAXA (Japan Aerospace Exploration Agency) and CSA (Canadian Space Agency) for formation flying using differential atmospheric drag though it hasn't been launched [1, 2]. The use of perturbation forces to maintain a formation has several advantages. It does not require a conventional propulsion system, which leads to mass savings. Moreover, because the accelerations generated by aerodynamic drag are relatively small, the technology is applicable to SFF missions with shock sensitive devices [2].

Thus far, the main contributions to this field can be classified into two areas. Researchers working in the first area aim to gain insight into the effect of the different perturbations of two satellites in an attempt to derive more precise relative motion equations. The other area of work is concerned with the development of a control algorithm to handle uncertainties and model inaccuracy in relative equations to maintain formation flying [3].

The equations that express the relative motion of satellites with respect to a circular orbit are known as the Hill-Clohessy–Wiltshire (HCW) equations [4]. These equations are derived as a set of linearized differential equations describing the relative motion of any two objects in near-circular orbits [5]. However, the HCW equations contain a great source of error in that Earth is assumed to be a perfect sphere. Several papers have contributed to the development of relative motion equations to incorporate the effects of various perturbations with significant effects on the relative motion [6–12]. These approaches involve different representations of relative states: translational relative states, curvilinear relative states, and orbital elements illustrating unperturbed and perturbed relative motion [13]. Important modifications in the translational states were achieved by Sedwick et al. [6]. He began his work by incorporating the J_2 effect for polar orbits. Schweighart and Sedwick then partially incorporated the mean motion of satellites into the relative motion equations by including the time average of the gradient of the J_2 potential to form a new set of constant coefficient linearized equations. Their model in [7] is referred to as the SS model in this paper. This model was further modified to provide a fairly accurate model of the cross-track motion under the influence of the J_2 potential in [8]. Finally, they linearized the trigonometric functions of cross-track motion for small-angle approximations [14].

Various control algorithms have been studied with the aim of enhancing the ability of satellites using aerodynamic drag to control the formation flying satellites. In 1989, Leonard et al. used a simple PID controller to achieve this goal [15]. Later, Hong et al. [16] developed an autonomous control method using a Lagrangian derivation that enables SFFs to successfully maintain their relative positions using aerodynamic drag. Jigang and Yulin [17] applied the phase plane when developing their control methods for co-planar motion. Bevilacqua et al. [18] proposed a two-phase hybrid controller to optimize propellant consumption by using thrust and aerodynamic drag for rendezvous missions. They designed the first phase to effect a propellant-free trajectory close to the target spacecraft using the differentials in aerodynamic drag, and then used a fuel-optimal control strategy via continuous low-thrust engines to effect precision docking. Kumar et al. [19] studied the maintenance of satellite formations using aerodynamic drag and solar radiation pressure separately, by integrating the results of a study of the modified HCW equations in [20] and the control methodology developed later [21]. Pastorelli and Bevilacqua [22] proposed a novel technique to utilize drag sails to control both the relative motion and orientation of satellites simultaneously for rendezvous missions. Cho et al. [23] designed a sliding mode controller using the SS model to achieve propellantless rendezvous missions by using differential aerodynamic drag. Mazal and Perez [24] derived simple Gaussian variational equations (GVE) to control rendezvous mission with uncertain parameters and subject to saturation by using differentials in the drag forces between spacecraft.

The differential in aerodynamic drag has been demonstrated to have the ability to alone eliminate the effects of different perturbations in in-plane motion for missions that need to maintain a formation in LEO [25]. The differential can also be used as the initial phase for rendezvous missions [18]; however, the integration of thrust and the differential in aerodynamic drag to derive a practical control algorithm for different formation flying missions has not been studied to the best of our knowledge. Our work is mainly concerned with designing a practical control algorithm to implement aerodynamic drag and thrust with different saturation levels to control the in-plane motion for various formation flying missions. First, when only atmospheric drag is implemented, the lack of the solvability of the tracking problem is pointed out. Then continuous thrust is integrated to ensure solvability and the stability region of the problem of formation flying is identified considering input saturation. A parameterized output regulation (POR) algorithm is designed to track the reference trajectories and eliminate the effects of different perturbations in the dynamics model. Semi-global stability is assured by using the parametric Lyapunov algebraic equation (PLAE), which is based on the low-gain state feedback theorem [26, 27] and parametric Lyapunov differential equation (PLDE) approach [28]. Input saturation can be included in the design process through parametric variation in PLAE. The control algorithm is numerically validated with the parameters of actual formation flying satellites (JC2Sat, Techsat21) by using the SS perturbed relative motion and high-precision orbit propagator (HPOP). The first contribution of our research to this state of the art is the integration between two different control actions to design a precise control algorithm for different reference trajectories. The derivation of a low conservative stable algorithm for parameterized output regulation for formation flying missions subject to different components of input saturation is the second achievement. The third contribution is the analysis of the performance of the PLAE control algorithm by using the SS relative model and HPOP numerical simulator.

In this paper, Section II presents the SS relative dynamics model. The differentials in aerodynamic drag and a method to implement the model for control action are explained in Sec. III. Section IV describes the development of the output regulation algorithm with PLAE and the stability conditions for combining the thrust and aerodynamic drag with different values of the saturation limits. Section V outlines the specifications of the numerical simulator and its built-in perturbation models. This section also presents test cases and their procedures. Subsequently, the performance of these test cases for the relative SS model is compared using the HPOP numerical simulator. The final section presents the conclusion of this paper and provides recommendations for future work. In this paper, the following notations are used for a vector-valued function $\boldsymbol{x}$ and $T \geq 0$.

$$\|\boldsymbol{x}\|_{\infty} = \sup_{t} \|\boldsymbol{x}(t)\| \ , \ \|\boldsymbol{x}\|_{\infty,T} = \sup_{t \geq T} \|\boldsymbol{x}(t)\|$$

where $\| \ . \ \|$ denotes the standard Euclidean norm.

II. Dynamics Models of Satellite Formation Flying

This section introduces the SS relative equations as a precise model, which is derived by incorporating the J_2 perturbation effects into the HCW relative dynamics model [29, 30]. The system of formation flying consists of leader (chief) and follower (deputy) satellites, where the SS equations describe the relative states between them in the Radial–Tangential-Normal (RTN) coordinate system. The final SS relative equations proposed in [8] are written as

$$\begin{aligned} \ddot{x} - 2nc\dot{y} - (5c^2 - 2)n^2 x &= a_x \\ \ddot{y} + 2nc\dot{x} &= a_y \\ \ddot{z} + q^2 z &= 2lq\cos\big(qt + \phi\big) + a_z \end{aligned} \tag{1}$$

where x, y, and z represent the relative difference in the position of the leader and follower under J_2 perturbation and n is the mean motion of the reference unperturbed circular orbit and is equal to $\sqrt{\mu / r_{ref}^3}$, where r_{ref} is the mean radius for the virtual reference circular orbit. This virtual reference orbit is defined by an unperturbed circular orbit with the equivalent orbital period of the leader satellite as presented in [8]. Parameters a_x, a_y, a_z are perturbations and control forces per unit mass in the x-, y-, and z-directions, respectively, and ϕ is the phase angle between the follower and leader satellites.

Because the control action of aerodynamic drag has no components in the out-of-plane motion as presented by Hajovsky [31], the in-plane motion of the SS model in Eq. (1) is treated in this paper. For this motion, the parameter c governs the natural frequency of the SS model, depending on the reference orbit inclination. c is defined as follows

$$c = \sqrt{1+s}$$
$$s = \frac{3J_2R_e^2}{8r_{ref}^2}\left(1 + 3\cos 2i_{ref}\right) \tag{2}$$

where i_{ref} is the inclination of the reference circular orbit, the geopotential constant J_2 is defined as the second spherical harmonics of Earth's geopotential, which is equal to 1.0826×10^{-3} and R_e is the mean radius of the Earth $R_e = 6.3781 \times 10^6$ m. The other parameters in Eq. (1) are related to the cross track motion as l, q and are defined elsewhere [8].

In this paper, the leader and follower satellites are placed in a "free-orbit ellipse". This ellipse describes the formation configuration in which the projection onto the in-plane motion is a two-by-one ellipse and forms a circle in three-dimensional motion [32]; however, it is necessary to modify the initial conditions to accommodate the SS model frequency. The initial velocity components $\dot{x}_0$ and $\dot{y}_0$ for the leader and follower satellites need to be adjusted to remove the secular motion and constant offset terms due to J_2 effects. Now, the initial values x_0, y_0, and z_0 and their derivatives for the SS model are given by

$$x_0 = \frac{r_{rel}}{2}\cos\phi,\ y_0 = r_{rel}\sin\phi$$
$$\dot{x}_0 = n\frac{1-s}{2\sqrt{1+s}}y_0,\ \dot{y}_0 = -2n\sqrt{1+s}x_0 \tag{3}$$

where r_{rel} is the initial formation radius. Based on these initial conditions, the analytical solution for the relative SS equations of in-plane motion becomes

$$x(t) = x_0\cos\left(nt\sqrt{1-s}\right) + \frac{\dot{x}_0}{n\sqrt{1-s}}\sin\left(nt\sqrt{1-s}\right)$$
$$y(t) = y_0\cos\left(nt\sqrt{1-s}\right) + \frac{\dot{y}_0}{n\sqrt{1-s}}\sin\left(nt\sqrt{1-s}\right) \tag{4}$$

where x_0 and y_0 represent the initial difference between the leader and follower.

III. Model of Aerodynamic Drag

Aerodynamic drag represents the largest non-gravitational force acting on LEO satellites. The magnitude of acceleration required to counteract the aerodynamic drag decreases dramatically according to the altitude of satellites compared to other perturbations [29]. This is why the use of aerodynamic drag to control formation flying is viable only for LEO satellites with altitudes less than 600 km. The differential in atmospheric drag between the leader and follower can be expressed as

$$\begin{aligned}\Delta \boldsymbol{f_d} &= \boldsymbol{f}_{\boldsymbol{d}_f} - \boldsymbol{f}_{\boldsymbol{d}_l} \\ &= -\frac{1}{2}\rho_f C_d \frac{A_f}{m_f} \boldsymbol{V}_{\boldsymbol{rel}_f} \left\| \boldsymbol{V}_{\boldsymbol{rel}_f} \right\| + \frac{1}{2}\rho_l C_d \frac{A_l}{m_l} \boldsymbol{V}_{\boldsymbol{rel}_l} \left\| \boldsymbol{V}_{\boldsymbol{rel}_l} \right\|\end{aligned} \tag{5}$$

where $\boldsymbol{f}_{\boldsymbol{d}_l}$ and $\boldsymbol{f}_{\boldsymbol{d}_f}$ are the aerodynamic drag force vectors for the leader and follower, respectively, $\boldsymbol{V}_{\boldsymbol{rel}_l}$ and $\boldsymbol{V}_{\boldsymbol{rel}_f}$ are the relative velocity vectors of the leader and follower with respect to the local atmosphere in the RTN coordinate system [20, 29], $\frac{A_l}{m_l}$ and $\frac{A_f}{m_f}$ are the areas over the mass ratio of the leader and follower, respectively, C_d is the drag coefficient, and ρ_l and ρ_f are the local aerodynamic densities of the leader and follower, respectively. In our study, the formation radius is assumed to be very small compared to the mean radius, hence we can assume that the relative velocities to the local atmosphere $\boldsymbol{V}_{\boldsymbol{rel}}$ for the leader and the follwer satellites are equal.

It is difficult to determine the exact values of the density in the upper aerodynamic layers, and many international standards attempt to promote one density model over another by specifying numerous parameters to select the best model for a particular mission and application [33, 34]. Among these models is the exponential density model (CIRA 72) [29], which we employed in our study, and which is expressed as follows

$$\rho = \rho_0 e^{\left(-\frac{h_{ellp} - h_0}{H}\right)} \tag{6}$$

where h_{ellp}, h_0, ρ_0 , and H are the actual altitude, base attitude, nominal density at the base attitude, and scale height, respectively [29].

Incorporating the attitude dynamics to calculate the cross-sectional area has the effect of complicating the derivation of the control algorithm. To reduce the complexity of the problem, the coordinate system of the satellite body is assumed to coincide with the RTN coordinate system of the reference orbit. The cross-sectional areas for the leader and follower satellites A_l and A_f are designed to be equal to

$$\begin{aligned}A_l &= A_{dl} \sin(\alpha_0 + \delta\alpha) \\ A_f &= A_{df} \sin(\alpha_0 - \delta\alpha)\end{aligned} \tag{7}$$

where A_{dl}, A_{df} are satellite drag plate areas for the leader and follower, respectively, α_0 is the initial rotation angle of the drag plates and $\delta\alpha$ is the change in the rotation angle due to the control action. The general form of actual drag plate angle of leader and follower satellites is α, which is equal to $\alpha_0 \pm \delta\alpha$. To simplify the problem, the follower and leader satellites are assumed to have the same drag plate areas, $A_d = A_{dl} = A_{df}$. Considering that only the drag plate areas contribute to the differential atmospheric drag, the difference in aerodynamic drag force becomes

$$\Delta \boldsymbol{f_d} = \rho C_d \frac{A_d}{m} \boldsymbol{V_{rel}} \|\boldsymbol{V_{rel}}\| \cos\alpha_0 \sin\delta\alpha \tag{8}$$

For a small formation radius, the velocity vector can be substituted by the scalar component in its tangential coordinate as

$$\boldsymbol{V_{rel}} = \begin{bmatrix} 0 & V_{rel} & 0 \end{bmatrix} \tag{9}$$

such that the control equation becomes

$$\Delta f_d = \rho C_d \frac{A_d}{m} V_{rel}^2 \cos\alpha_0 \delta\hat{\alpha} \tag{10}$$

where $\delta\hat{\alpha}$ is a presentation for $\sin\delta\alpha$.

This configuration for implementing drag plates to control the relative position is presented in Fig. 1, where the black solid lines of the drag plates indicate the initial orientation α_0 and the blue lines represent the actual orientation of the drag plates $\alpha_0 \pm \delta\alpha$. Figure 1(a) illustrates the configuration for $\Delta f_d > 0$, where the leader's drag plate angle α_l increases with a consequent increase in its aerodynamic drag force f_{d_l} and the follower drag plate angle α_f decreases with a consequent decrease in its aerodynamic drag force f_{d_f}. Figure 1(b) presents the opposite configuration for $\Delta f_d < 0$. It should be noted that the assumption that both satellites have the same density and relative velocities is valid only for missions flying in close formation with a formation radius $r \leq 10$ km [19].

IV. Output Regulation for Linear Time-Invariant Systems

The objective of the output regulation problem is to find a feedback control setting such that the output of the system converges to zero as time tends to infinity. This problem can be used to

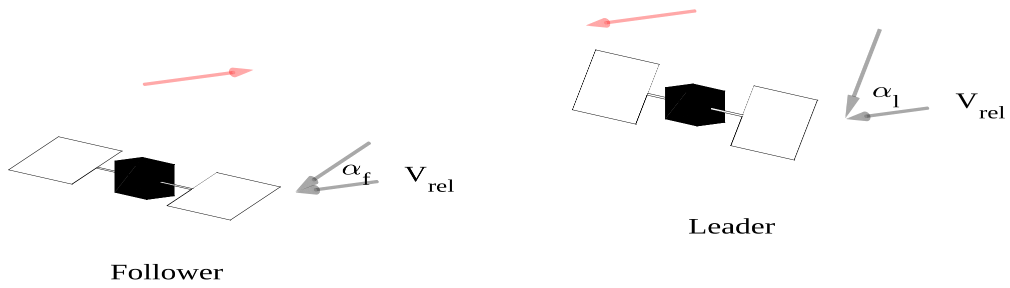

(a) $\delta\alpha > 0$

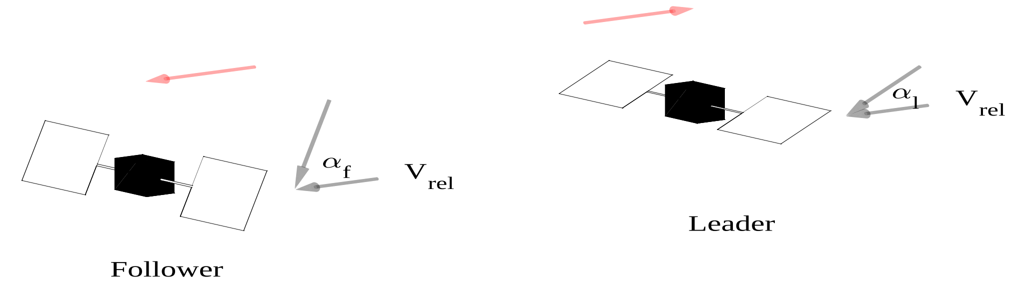

(b) $\delta\alpha < 0$

Fig. 1: Configuration of drag plates: (a) $\Delta f_d > 0$, (b) $\Delta f_d < 0$

model asymptotic tracking as well as asymptotic disturbance rejection. The dynamic equations, including those of an exogenous system, can be stated as follows

$$\begin{aligned} \dot{\boldsymbol{x}}(t) &= A\boldsymbol{x}(t) + B_1\boldsymbol{\omega}(t) + B_2\boldsymbol{u}(t) \\ \dot{\boldsymbol{\omega}}(t) &= S\boldsymbol{\omega}(t) \\ \boldsymbol{e}(t) &= C\boldsymbol{x}(t) + D_{11}\boldsymbol{\omega}(t) + D_{12}\boldsymbol{u}(t) \end{aligned} \tag{11}$$

where $\boldsymbol{x} \in \mathbb{R}^n$ is the state vector, $\boldsymbol{u} \in \mathbb{R}^m$ is the control input, $\boldsymbol{e} \in R^l$ is the output to be regulated, and $\boldsymbol{\omega} \in \mathbb{R}^d$ is the reference signal or external disturbances generated by an antistable exosystem. The full-information output regulation problem is solvable, if and only if $(A,\ B_2)$ is stabilizable and there exist control gain matrices $\Pi(\in \mathbb{R}^{n\times d})$ and $\Gamma(\in \mathbb{R}^{d\times d})$, which satisfy the regulator equation [35].

$$\begin{aligned} \Pi S &= A\Pi + B_2\Gamma + B_1 \\ 0 &= C\Pi + D_{12}\Gamma + D_{11} \end{aligned} \tag{12}$$

For clarity, we assume $D_{12} = 0$. Under these conditions, admissible controllers are given by

$$\boldsymbol{u}(t) = K\boldsymbol{x}(t) + L\boldsymbol{\omega}(t) \tag{13}$$

where K is any matrix such that $A + B_2K$ is Hurwitz stable and $L = \Gamma - K\Pi$. As seen in Eq. (13), the control input mainly consists of two parts: $K\boldsymbol{x}$, which is the feedback term used to steer $\boldsymbol{x}$ to $\boldsymbol{\omega}$, and $L\boldsymbol{\omega}$, which is the feedforward term to adjust for the trajectory frequency. Equation (13) can be rewritten as

$$\boldsymbol{u}(t) = K\hat{\boldsymbol{x}}(t) + \Gamma\boldsymbol{\omega}(t) \tag{14}$$

where $\hat{\boldsymbol{x}} = \boldsymbol{x} - \Pi\boldsymbol{\omega}$. Using $\hat{\boldsymbol{x}}$ and $\boldsymbol{\omega}$, the output signal $\boldsymbol{e}(t)$ is given by

$$\boldsymbol{e}(t) = C\boldsymbol{e}^{(A+B_2K)t}\hat{\boldsymbol{x}}_0 + (C\Pi + D_{11})e^{St}\boldsymbol{\omega}_0 \tag{15}$$

From the regulator equation (12), the second term in the left hand side of Eq.(15) is zero. Therefore, output regulation is achieved, i.e., $\lim_{t\to\infty} \boldsymbol{e}(\boldsymbol{t}) = 0$.

A. Control input saturation

This subsection considers the stability of the output regulation problem subject to input saturation with different saturation values. The analysis can easily be generalized to a vector input case with the following state space representation

$$\begin{aligned} \dot{\boldsymbol{x}}(t) &= A\boldsymbol{x}(t) + B_1\boldsymbol{\omega}(t) + B_2\boldsymbol{\mu}_\infty\sigma(\boldsymbol{u}(t)) \\ \dot{\boldsymbol{\omega}}(t) &= S\boldsymbol{\omega}(t) \\ \boldsymbol{e}(t) &= C\boldsymbol{x}(t) + D_{11}\boldsymbol{\omega}(t) \end{aligned} \tag{16}$$

Parameter $\sigma(\boldsymbol{u}(t))$ is the normalized saturation function to assure $\left\|\sigma(\boldsymbol{u}(t))\right\|_\infty \leq 1$, and it is defined as

$$\sigma(u_i(t)) = \begin{cases} \frac{u_i}{\mu_{\infty_i}} & if \;\; |u_i| \leq \mu_{\infty_i} \\ 1 & if \;\; u_i > \mu_{\infty_i} \\ -1 & if \;\; u_i < -\mu_{\infty_i} \end{cases} \tag{17}$$

The coefficient matrix $\boldsymbol{\mu}_\infty \in \mathbb{R}^{m \times m}$ represents the saturation limits for different control inputs, which is stated as follows

$$\boldsymbol{\mu}_\infty = \begin{bmatrix} \mu_{\infty_1} & & 0 \\ & \ddots & \\ 0 & & \mu_{\infty_m} \end{bmatrix} \tag{18}$$

The solvability conditions for the output regulation problem for linear systems subject to input saturation are given in the following Theorem.

Theorem 1 [27]: Consider system (16) and the given compact set $\boldsymbol{W_0} \subset \mathbb{R}^d$. The classical semi-global linear state feedback output regulation problem is solvable if the following conditions hold:

(i) $(A,\ B_2)$ is stabilizable and A has all its eigenvalues in the closed left half plane.

(ii) There exist matrices Π and Γ such that:

(a) they solve output regulator equation (12) i.e.,

$$\begin{aligned} \Pi S &= A\Pi + B_2\Gamma + B_1 \\ 0 &= C\Pi + D_{12}\Gamma + D_{11} \end{aligned} \tag{19}$$

(b) there exists $0 < \delta < 1$ and $T \geq 0$ such that $\|\Gamma\boldsymbol{\omega}\|_{\infty,T} \leq (1-\delta)$ for all $\boldsymbol{\omega}$ with $\boldsymbol{\omega}(0) \in \boldsymbol{W_0}$.

One way to select such a state feedback is to use a parameterized feedback gain matrix. Previously [27, 36], the Riccati equation

$$P_\varepsilon A + A^T P_\varepsilon - P_\varepsilon B_2 R^{-1} B_2^T P_\varepsilon + Q_\varepsilon = 0 \tag{20}$$

where $Q_\varepsilon = \varepsilon I$ and $R > 0$, was used to construct a family of linear state feedback parameterized in ε. The important properties of the parameterized Riccati equation (20) are that $Q_\varepsilon > 0$, $\frac{dQ_\varepsilon}{d\varepsilon} > 0$ for any $\varepsilon \in (0, 1]$ and $\lim_{\varepsilon \to 0} Q_\varepsilon = 0$.

However, it is known that solving the parameterized Riccati equation might be numerically stiff as stated in [27]. Furthermore, the convergence of $e(t)$ using low-gain feedback is also known to be very slow due to the restrictions on parameterized gains [26].

To overcome these difficulties in solving the parameterized Riccati equation, we propose the use of a parameterized Lyapunov algebraic equation (PLAE). Let P_ε be a unique positive definite solution of the Riccati equation (20) with $Q_\varepsilon = \varepsilon P_\varepsilon$, then $W_\varepsilon = P_\varepsilon^{-1}$ is the unique positive definite solution to the following PLAE:

$$0 = A_\varepsilon^T W_\varepsilon + W_\varepsilon A_\varepsilon + C_1^T C_1 \tag{21}$$

where $A_\varepsilon = -A^T - \frac{1}{2}\varepsilon I_n$ and $C_1 = R^{-\frac{1}{2}} B_2^T$. This solution can generate a stable feedback gain $K_\varepsilon = -R^{-1}B_2^T P_\varepsilon$, while assuring the boundedness of the magnitude of state feedback [28]. Moreover, the properties $Q_\varepsilon > 0$, $\frac{dQ_\varepsilon}{d\varepsilon} > 0$ for any $\varepsilon \in (0, \varepsilon^*]$, and $\lim_{\varepsilon \to 0} Q_\varepsilon = 0$ hold (see Appendix A).

Therefore, if the parameter ε is sufficiently small to assure the conditions of the developed PLAE approach, then the output regulation subject to the input saturation is achieved by

$$\boldsymbol{u}(t) = K_\varepsilon \boldsymbol{x}(t) + L\boldsymbol{\omega}(t) \tag{22}$$

where $L = \Gamma - K_\varepsilon \Pi$.

This implementation of the PLAE mainly aims to ensure that the parameterized equations are less numerically stiff and to raise the limit for the parameter ε while approving the stability conditions. Moreover, the solution P_ε can be solved analytically for a linear time-invariant (LTI) system.

B. Formation flying using thrust and aerodynamic drag

The main reason for applying the output regulation problem is the viability of using aerodynamic drag as a practical way to control various formation flying missions subject to input saturation. This cannot be precisely controlled by using any other linear control algorithm. Stability analysis was conducted for various reference trajectories. In-plane formation flying using only aerodynamic drag is fully controllable [25] for rendezvous and formation keeping missions. However, tracking control for in-plane motion cannot be fully solved as pointed out below.

Control of in-plane formation flying should incorporate control action in the x-direction to achieve full solvability of the output regulation problem. In our problem, this control action is implemented as thrust. For the SS model, the matrices A, B_1 and B_2 in Eq. (16) are given by

$$A = \begin{bmatrix} 0 & 0 & 1 & 0 \\ 0 & 0 & 0 & 1 \\ \left(5c^2 - 2\right)n^2 & 0 & 0 & 2nc \\ 0 & 0 & -2nc & 0 \end{bmatrix},\ B_1 = 0,\ B_2 = \begin{bmatrix} 0 & 0 \\ 0 & 0 \\ 1 & 0 \\ 0 & B_y \end{bmatrix} \tag{23}$$

where $B_y = \rho C_d \frac{A}{m} V_{rel}^2 \cos\alpha_0$ and $u = \begin{bmatrix} u_x & \delta\hat{\alpha} \end{bmatrix}^T$ is the control input for the leader and follower satellites, where $\|\boldsymbol{x}\|_\infty = r_{rel}$, which represents the initial formation radius. Moreover, the free orbit ellipse is generated by

$$\dot{\boldsymbol{\omega}} = S\boldsymbol{\omega},\ \boldsymbol{\omega}(0) = \boldsymbol{\omega}_0$$

For the tracking problem, matrices C, D_{11}, and D_{12} become

$$C = \begin{bmatrix} 1 & 0 & 0 & 0 \\ 0 & 1 & 0 & 0 \end{bmatrix},\ D_{11} = \begin{bmatrix} -1 & 0 \\ 0 & -1 \end{bmatrix},\ D_{12} = 0 \tag{24}$$

To satisfy $\boldsymbol{\omega}(\tau) = \begin{bmatrix} a\cos\omega_{ref}\tau & b\sin\omega_{ref}\tau \end{bmatrix}^T$, S needs to satisfy

$$S = \begin{bmatrix} 0 & S_1 \\ S_2 & 0 \end{bmatrix} \tag{25}$$

where $S_1 = \frac{-a\omega_{ref}}{b}$ and $S_2 = \frac{b\omega_{ref}}{a}$, hence $S_1S_2 = -\omega_{ref}^2$. The output regulation problem is solvable because the matrix

$$A_1 = \begin{bmatrix} A - \lambda I & B_2 \\ C & D_{12} \end{bmatrix}$$

has full rank for each eigenvalue λ of S [37]. It should be noted that the output regulation problem is not solvable when only atmospheric drag is used. This can be confirmed by replacing B_2 in Eq. (23) by $B_2 = \begin{bmatrix} 0 & 0 & 0 & B_y \end{bmatrix}^T$.

This problem is considered as a full-information problem with state feedback; therefore, actual state $\boldsymbol{x}$ and reference trajectory state $\boldsymbol{\omega}$ are available for control. For the formation flying problem (Eqs. (23) and (24)), solutions to the regulator equation (19) are explicitly given by

$$\Pi = \begin{bmatrix} 1 & 0 \\ 0 & 1 \\ 0 & -\frac{a\omega_{ref}}{b} \\ \frac{b\omega_{ref}}{a} & 0 \end{bmatrix}, \ \Gamma = \begin{bmatrix} -\frac{a\omega_{ref}^2 + an^2(5c^2-2)+2bnc\omega_{ref}}{a} & 0 \\ 0 & -\frac{b\omega_{ref}^2+2nca\omega_{ref}}{bB_y} \end{bmatrix} \tag{26}$$

Now the explicit expressions for $\boldsymbol{\mu}_\infty, \delta$, and P_ε in the PLAE approach are derived for each combination of the thrust and differentials in aerodynamic drag, where weighting matrices $Q_\varepsilon = \varepsilon P_\varepsilon$. We choose $R = \begin{bmatrix} 1 & 0 \\ 0 & B_y^2 \end{bmatrix}$ to normalize the input part of the cost function $u^T R u$, where the matrix $\boldsymbol{\mu}_\infty$ is equal to

$$\boldsymbol{\mu}_\infty = \begin{bmatrix} u_{max} & 0 \\ 0 & \alpha_0 \end{bmatrix} \tag{27}$$

where u_{max}, α_0 are the saturation limits of thruster and atmospheric drag control actions respectively. The saturation limit for atmospheric drag α_0 is selected so that the normalized control action of differential atmospheric drag is existed in the subset $[-1, 1]$ and this implies that $\|\delta\alpha\|_\infty \leq |\alpha_0| \leq \pi/4$. On the basis of the free-ellipse initial conditions of formation trajectories Eq. (3), the reference trajectory vector can be stated as follows

$$\boldsymbol{\omega} = \begin{bmatrix} \frac{r}{2}\cos\omega_{ref}\tau & r\sin\omega_{ref}\tau \end{bmatrix}^T \tag{28}$$

where r, ω_{ref} are the magnitude and the frequency of the reference trajectory, respectively. We can substitute $\omega_{ref} = Dn$, where D presents the constant frequency factor, to illustrate the relation between the reference trajectory frequency and unperturbed HCW frequency. On the other hand, from Theorem 1, we have $\|\Gamma\boldsymbol{\omega}\|_{\infty,T} \leq 1 - \delta$, where $\| \ \|_{\infty,T}$ denotes the L_∞-norm after time T. This means that

$$\delta < \min\left\{1 - \left|\frac{n^2 r}{2u_{max}}(D^2 - 4cD + (5c^2-2))\right|, 1 - \left|\frac{n^2 r}{B_y\alpha_0}(D^2 - cD)\right|\right\} \tag{29}$$

Test cases are mainly set for JC2Sat satellites with their physical parameters provided in Table 1 [1, 2], while u_{max} is set to be 0.1 mN.

Table 1: Parameters of JC2Sat

Parameter	Symbol	Unit	Value
Mass	M	kg	18
Drag Plate Area	A_d	m^2	0.09
Drag Coefficient	C_d	−	2.2

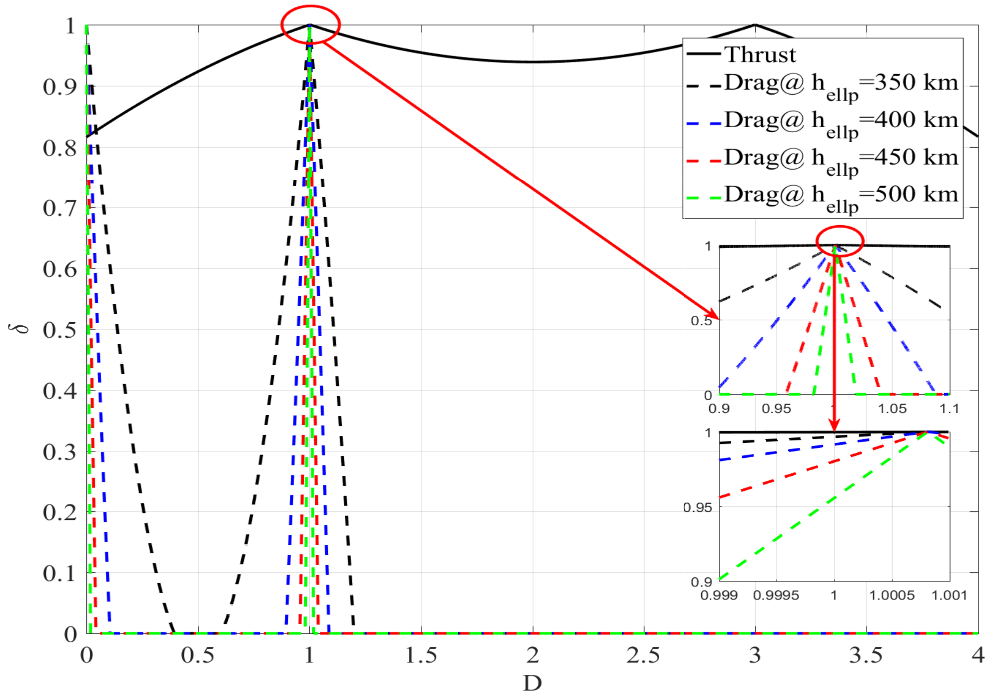

Fig. 2: Simulation of δ values for different frequencies factors D for altitudes $h_{ellp} = 350, 400, 450, 500$ km for JC2Sat

Figure 2 presents the relation between frequency factor D and δ, which is the ratio of feedback control action $\|K\hat{x}\|_\infty$ to the saturation value of the control input as presented in Theorem 1, with $|c| \approx 1$, mean radius for the virtual reference circular orbit $r_{ref} = R_e$ and initial drag plate angle $\alpha_0 = \pi/4$. If it is equal to zero, it means that there is no feedback action $K\hat{x}$ to eliminate the error signal and if it is equal to one, it means that there is no output regulation action $\Gamma\omega$ to track the reference trajectory.

The results in Fig. 2 show that the margin of reference frequencies that can be achieved using

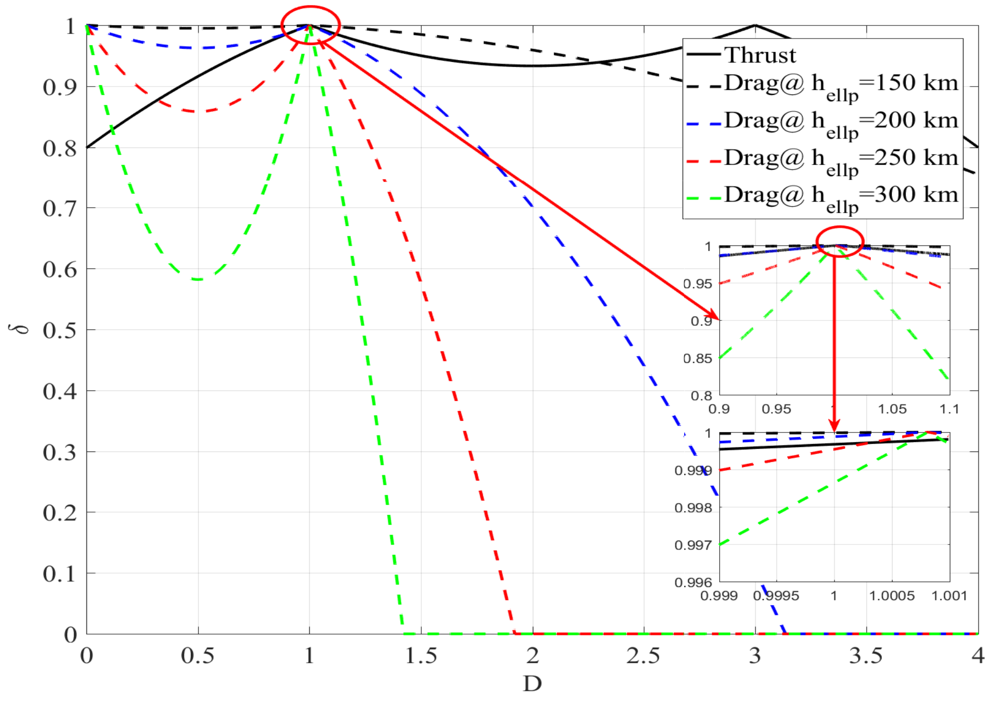

Fig. 3: Simulation of δ values for different frequencies factors D for altitudes $h_{ellp} = 150, 200, 250, 300$ km for JC2Sat

aerodynamic drag and thrust for JC2Sat satellites at altitudes $h_{ellp} \in [350, 500]$ is highly restricted, where a change of approximately 5% in frequency factor D leads to saturation of the control action for altitudes $h_{ellp} = 450$ and 500 km, whereas it decreases the available control action for feedback $K\hat{x}$ to more than 50% and 20% of its total value at altitudes $h_{ellp} = 400$ and 350 km, respectively. The restriction on frequency can be relaxed by considering two methods

1. Decreasing the reference altitudes.

2. Increasing the area-to-mass ratio.

Figure 3 shows the result of the first approach by decreasing the altitude to $h_{ellp} = 150 - 300$ km . As shown in Fig. 3, the margin of frequency value ω_{ref} at altitude $h_{ellp} = 150$ km is expanded to be $\omega_{ref} > 4n$, whereas for $h_{ellp} = 500$ km it is approximately equal to $\omega_{ref} = 1.018n$ as presented in Fig. 2.

Figure 4 shows the result of the second approach where the area-to-mass ratio increases from

Table 2: Parameters of Techsat21

Parameter	Symbol	Unit	Value
Mass	M	kg	175
Drag Plate Area	A_d	m^2	2.22
Drag Coefficient	C_d	–	2.3

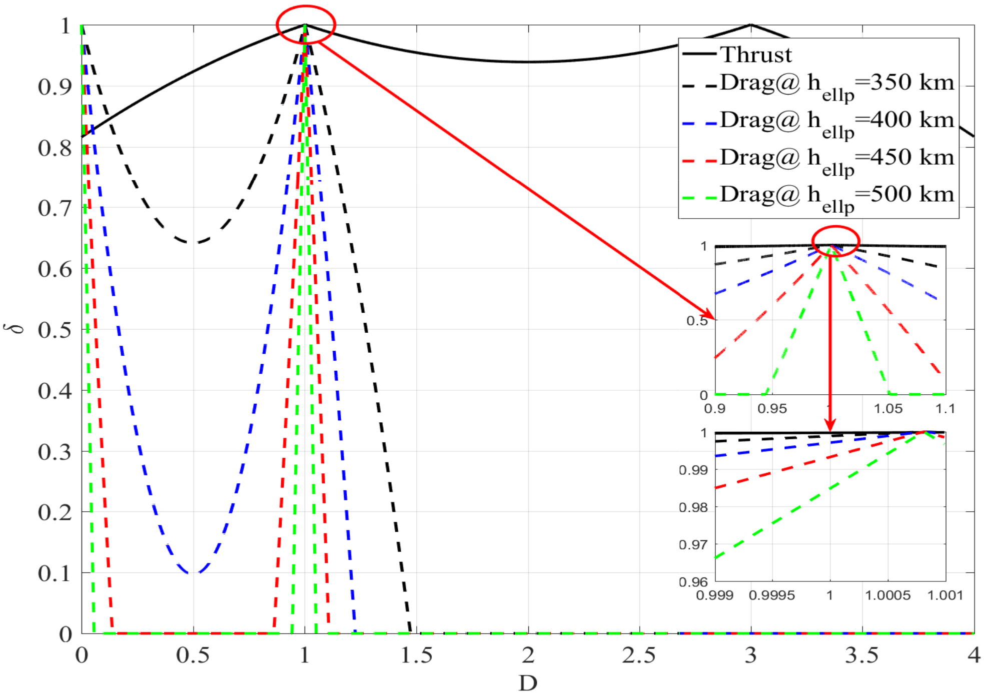

Fig. 4: Simulation of δ values for different frequencies factors D for altitudes $h_{ellp} = 350, 400, 450, 500$ km for Techsat21

0.005 for JC2Sat (Table 1) to 1.269×10^{-2} of Techsat21 (Table 2). As shown in Figs. 2 and 4, the marginal frequency increases from $\omega_{ref} = 1.2n$ to $\omega_{ref} = 1.474n$ for altitude $h_{ellp} = 350$ km. For the feedback, the solution to the parameteric Lyapunov algebraic equation (PLAE) is explicitly obtained by using the Sylvester equation and Kronecker product for symmetric matrices [38]. The PLAE approach presents a minimally conservative and low numerically stiffness approach to achieve semi-global stability of linear time invariant systems subject to different input saturation limits. It is derived with the parameterized Lyapunov equation that can be solved analytically for any generalized state representation form. The control gain is given by

$$K_\varepsilon = -B_2^T R^{-1} P_\varepsilon = \frac{1}{W_n} \begin{bmatrix} K_{11} & K_{12} & K_{13} & K_{14} \\ \frac{K_{21}}{B_y} & \frac{K_{22}}{B_y} & \frac{K_{23}}{B_y} & \frac{K_{24}}{B_y} \end{bmatrix} \tag{30}$$

where

$$\begin{aligned}
W_n =& \varepsilon^8 + \left(6\,M^2 - 4\,N\right)\varepsilon^6 + \left(9\,M^4 - 8\,M^2N + 6\,N^2\right)\varepsilon^4 \\
&+ \left(4\,M^6 - 4\,M^4N + 10\,M^2N^2 - 4\,N^3\right)\varepsilon^2 + 4\,\left(M^2 - N/2\right)^2 N^2 \\
K_{11} =& -\varepsilon^{10} - \left(6\,M^2 - 4\,N\right)\varepsilon^8 - \left(9\,M^4 - M^2N + 6\,N^2\right)\varepsilon^6 \\
&- \left(4\,M^6 + 7\,M^4N + 10\,M^2N^2 - 4\,N^3\right)\varepsilon^4 - \left(4\,M^6N + 4\,M^4N^2 - 3\,M^2N^3 + N^4\right)\varepsilon^2 \\
K_{12} =& M\left(M^2 + \varepsilon^2 - N\right)\varepsilon^3\left(4\,M^4 + 5\,M^2\varepsilon^2 + \varepsilon^4 - N^2\right) \\
K_{13} =& -2\,\varepsilon^9 - \left(12\,M^2 - 8\,N\right)\varepsilon^7 - \left(18\,M^4 - 10\,M^2N + 12\,N^2\right)\varepsilon^5 \\
&- \left(8\,M^6 - 2\,M^4N + 16\,M^2N^2 - 8\,N^3\right)\varepsilon^3 - \left(4\,M^4N^2 - 6\,M^2N^3 + 2\,N^4\right)\varepsilon \\
K_{14} =& \varepsilon^2 MN\left(2\varepsilon^4 - (2\,M^2 + 4N)\varepsilon^2 - 4M^4 - 4M^2N + 2N^2\right) \\
K_{21} =& -\,\varepsilon^8 - \left(6\,M^2 - 7\,N\right)\varepsilon^6 - \left(9\,M^4 - 11\,M^2N + 11\,N^2\right)\varepsilon^4 \\
&- \left(4M^6 - 4M^4N + 19\,M^2N^2 - 5\,N^3\right)\varepsilon^2 - 8\,M^4N^2 + 4M^2N^3 \\
K_{22} =& -\varepsilon^2\left(\varepsilon^6 + \left(5\,M^2 - 3\,N\right)\varepsilon^4 + \left(4M^2 - 3\,N\right)\left(M^2 - N\right)\varepsilon^2 - N\left(2M^2 - N\right)^2\right) \\
&\cdot\left(\varepsilon^2 + M^2 - N\right) \\
K_{23} =& \varepsilon^2 MN\left(2\varepsilon^4 - (2\,M^2 + 4N)\varepsilon^2 - 4M^4 - 4M^2N + 2N^2\right) \\
K_{24} =& -2\,\varepsilon^9 - \left(12\,M^2 - 8N\right)\varepsilon^6 - \left(18\,M^4 - 22\,M^2N + 12\,N^2\right)\varepsilon^4 \\
&- \left(8M^6 - 14\,M^4N + 24\,M^2N^2 - 8N^3\right)\varepsilon^2 - \left(12\,M^4N^2 - 10\,M^2N^3 + 2\,N^4\right)
\end{aligned} \tag{31}$$

for $M = 2nc$ and $N = n^2(5c^2 - 2)$.

In Fig. 2, for $D = 1$, the value of δ changes from 99.69% to 95.97%, which guarantees a stable region for feedback control action $\|K_\varepsilon \hat{\boldsymbol{x}}\|_\infty \leq \delta$, where $\|\hat{\boldsymbol{x}}\|_\infty \leq (r_{rel} + r)$.

At this point, the stability ranges of control parameter ε^* for different reference orbits are analyzed by using the PLAE approach. Figure 5 shows the relation between ε and the L_∞-norm of $K_\varepsilon \hat{\boldsymbol{x}}$ for different altitudes ($h_{ellp} \in [350, 500]$) with JC2Sat parameters, initial formation radius $r_{rel} = 100$ m, reference formation radius $r = 10$ m , and reference frequency $\omega_{ref} = n$. Figure 5

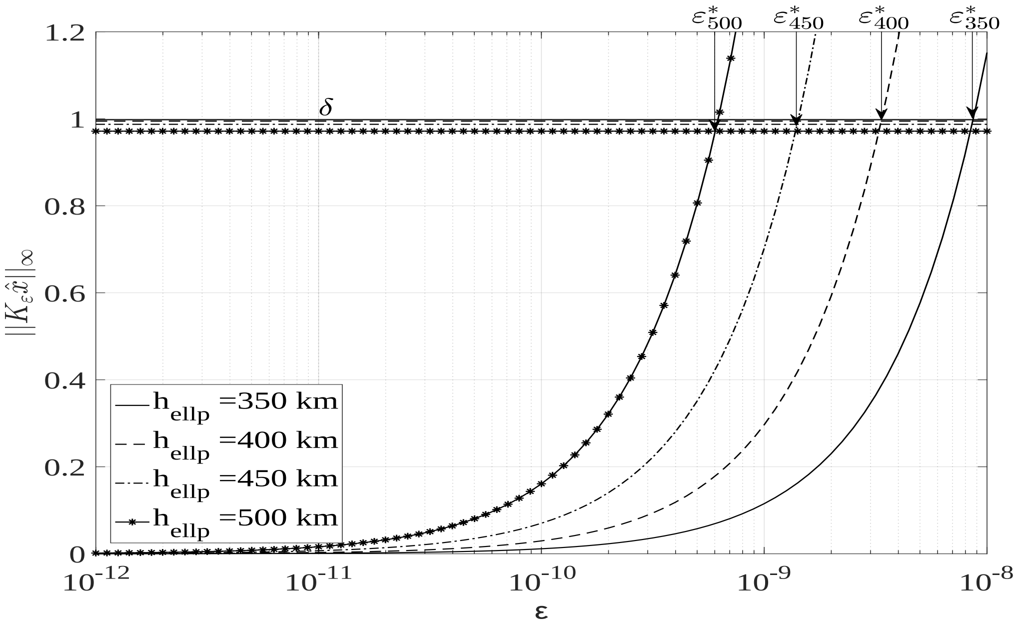

Fig. 5: Simulation of PLAE approach for maximum values for ε with ε^* conditions.

illustrates the limits of stable control gains, which are estimated using PLAE approach by calculating L_∞-norm of $K_\varepsilon \hat{\boldsymbol{x}}$. The $K_\varepsilon \hat{\boldsymbol{x}}$ curves monotonically increase as the altitude increases. From Fig. 5, it can be seen that the limits of ε^*_x for all altitudes $h_{ellp} \leq 500$ km are larger than 6×10^{-10}.

V. Simulation Results

A. Relative Model

This subsection examines the effect of the control parameter ε on the steady-state error and the corresponding control action for the SS model. The performance of parameterized control action (22) is tested for a circular LEO with different altitudes $h_{ellp} \in [350, 500]$ and inclination $i_{ref} = 0$, which represents the greatest effect of the J_2 perturbation force on the SS model. The propagation runtime was obtained for a period of 30 days for each test case with the time step $h = 10$ seconds. The numerical simulations were carried out in conjunction with the proposed output regulation controller and LQR controller. Test cases were specified for JC2Sat satellites with their physical parameters listed in Table 1 [1, 2].

The remaining orbital elements of the follower satellite i_f, Ω_f, and M_f were calculated according to the equations of the SS model presented in [8]. Furthermore, the initial formation radius $r_{rel} = 100$ m, reference formation radius $r = 10$ m , and phase angle $\phi = 45$ deg were used.

Let the in-plane state of the SS model (1) and reference trajectory (28) be $\delta\boldsymbol{x}$ and $\delta\boldsymbol{x}_{ref}$, respectively. Then the L_2-norm of the steady-state error is defined as

$$\nu_2 = \left\| W \left(\delta\boldsymbol{x}(t_i) - \delta\boldsymbol{x}_{\boldsymbol{ref}}(t_i) \right) \right\|_2, \ t_i \in \left[t_{ss}, t_f \right] \tag{32}$$

where W is a weighting matrix given by $W = diag\left(1, 1, n^{-1}, n^{-1}\right)$ [13] and t_{ss}, t_f are the settling time and final time, respectively.

Figure 6 shows the L_2-norm of the steady-state error (32) as a function of $q = \log_{10} \varepsilon$ for different altitudes h_{ellp}. All the results in Figs. 6(a) and 6(b) present a monotonically decreasing function for q in both figures. Although the control action of aerodynamic drag increases as the altitude decreases, at lower altitudes the error becomes larger because of increasing J_2 perturbation effects in the SS model. The control actions for the steady-state signal can be expressed as

$$\begin{aligned} \|u_x\|_2 &= \left\| K_1 \hat{\boldsymbol{x}}(t_i) + \Gamma_1 \omega(t_i) \right\|_2, \ t_i \in \left[t_{ss}, t_f \right] \\ \|\delta\hat{\alpha}\|_2 &= \left\| K_2 \hat{\boldsymbol{x}}(t_i) + \Gamma_2 \omega(t_i) \right\|_2, \ t_i \in \left[t_{ss}, t_f \right] \end{aligned} \tag{33}$$

Figures 7 and 8 present the L_2-norm of the control input for the steady state as a function of q for the parameterized linear quadratic regulator (PLQR) and the parametrized output regulation (POR) for various altitudes, where the limits of the normalized feedback control action for the PLQR is estimated by $\|K_\varepsilon \hat{\boldsymbol{x}}\|_\infty \leq 1$ and $K_\varepsilon = -R^{-1} B_2^T P_\varepsilon$, where P_ε is the solution to the Riccati equation (20). In Fig. 8, for the PLQR control, the steady-state control action increases dramatically as the control gain increases, because $\lim_{t \to \infty} \boldsymbol{e} \neq 0$ for the periodic trajectory. On the other hand, this does not occur for output regulation as presented in Fig. 7 because $\lim_{t \to \infty} \boldsymbol{e} = 0$. The steady state control action is equal to $\Gamma\omega$, which is independent of q; hence, the steady-state control action is constant for all q and for each altitude.

Both Fig. 7(b) and Fig. 8(b) show that, the higher the altitude becomes, the more the L_2-norm of $\delta\alpha$ increases. This is because an increase in the altitude h_{ellp} leads to a decrease in density ρ as presented in Eq. (6), which means that the control action $\delta\alpha$ should be increased to compensate for the reduction in density. Conversely, Figs. 7(a) and 8(a) present a negative correlation between

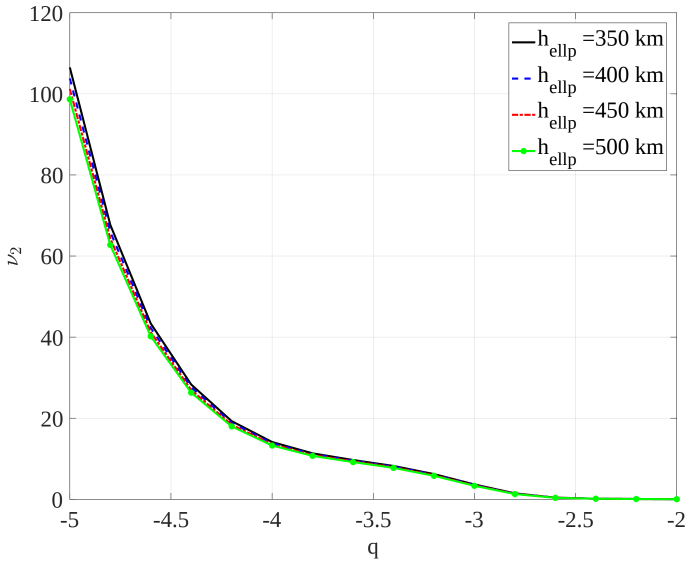

(a) Parameterized linear quadratic regulator (PLQR)

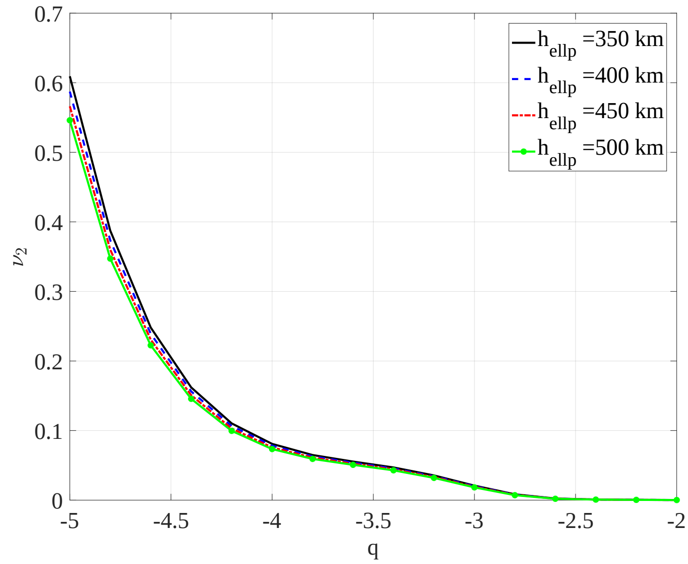

(b) Parameterized output regulator (POR)

Fig. 6: L_2-norm of steady state error w.r.t different weighting factor q and different altitudes for (a) PLQR (b) POR

u_x and the altitude h_{ellp}, which is attributed to the decrease in the perturbation effects of J_2 as the altitude increases. This leads to a reduction in the required control action by thrust; however, this reduction in the J_2 perturbation effect is lower than the reduction in the aerodynamic density value [29], which means that the control action $\delta\alpha$ increases. The results in Fig. 6 show that, when using the output regulation control, the L_2-norm of the steady-state error is reduced to less than 0.6, which represents an error of less than 1% of that of the PLQR algorithm. In contrast, the control action for both control algorithms remains at the same level as presented in Figs. 7 and 8

Figures 7 and 8 suggest that the stability conditions for the control parameter ε^* of the PLAE approach established in Sec. IV B is highly restrictive in comparison with numerical simulation. Figure 6 shows that the effect of saturation can be accommodated for $q \leq -2$ for all altitudes, whereas it is restricted by $q \leq -8$ for the stability analysis presented in Sec. IV B.

B. High Precision Orbit Propagator

This section presents the implementation of our control algorithm in the high precision orbit propagator (HPOP). The same procedure is applicable to the real space environment to demonstrate its viability to eliminate perturbations that have not been modeled.

The HPOP is based on AstroLib software [39], which incorporates high-fidelity force models, a high-accuracy numerical integrator, and precise transformation for both time scales and reference systems. It is used as benchmark for the verification and validation of the performance of the control algorithm. The description of the force models and numerical integration method implemented in AstroLib software is presented in Table 3. The test cases for HPOP simulation are designed for JC2Sat parameters with altitudes $h_{ellp} = 250, 300, 350$ and 400 km, reference inclination $i_{ref} = 0$, control weighting factor $\varepsilon = 10^{-4}$, and for the same initial and reference formation flying trajectories in Sec. V A.

The procedure that was used to test the feedback control system is shown in Fig. 9, where $\widetilde{oe}$ represents the oscillatory orbital elements (semi-major axis a, eccentricity e, inclination i, right ascension of ascending node Ω, argument of perigee ω, and mean anomaly M), $\boldsymbol{x}$ is the relative position vector, $\boldsymbol{u}$ is the control action vector $\boldsymbol{u} = [u_x, \delta\alpha]$, and Δ represents the difference between vectors of the actual and reference states. The subscripts $(2 - body, HPOP, f, l, ref)$ denote the two-body orbit propagator, high-precision orbit propagator, follower, leader, and reference trajectory, respectively. The superscripts (ECI, RTN) refer to the Earth-centered inertial and RTN

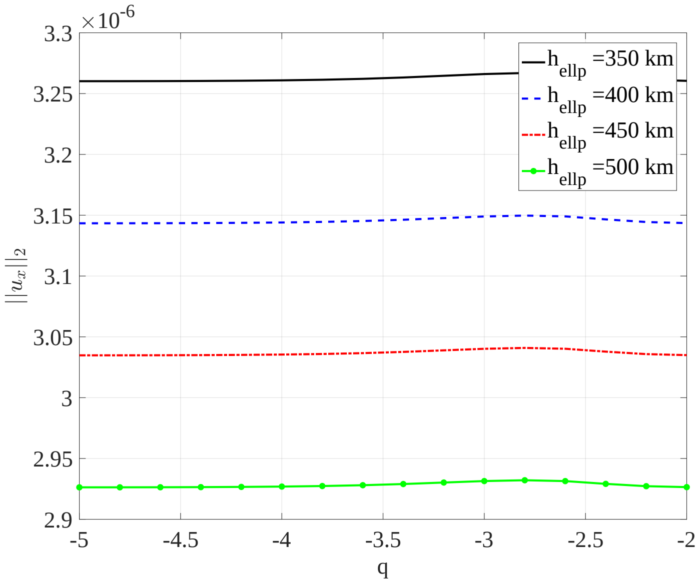

(a) u_x

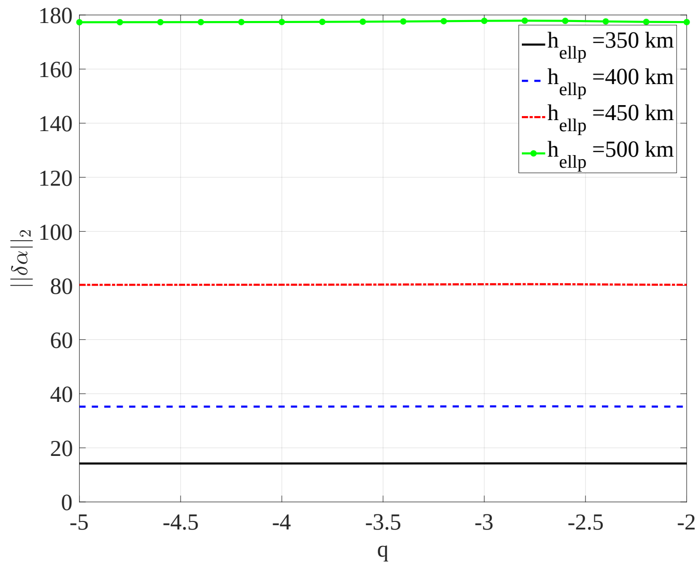

(b) $\delta\alpha$

Fig. 7: L_2-norm of output regulation actions u_x and $\delta\alpha$ as a function of weighting factor q for (a) L_2-norm of u_x (b) L_2-norm of $\delta\alpha$

coordinate systems, respectively [29].

The sequence of the closed-loop verification procedure starts with the transformation of the initial leader oscillatory orbital elements to the state described in the ECI coordinate system. These

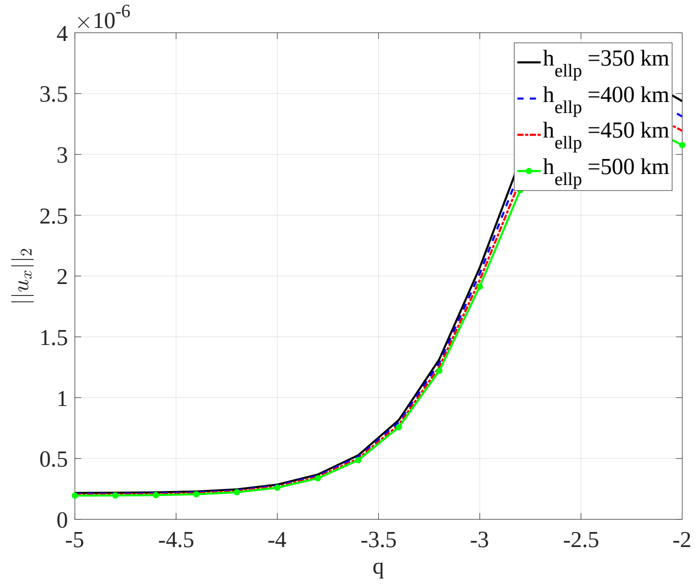

(a) u_x

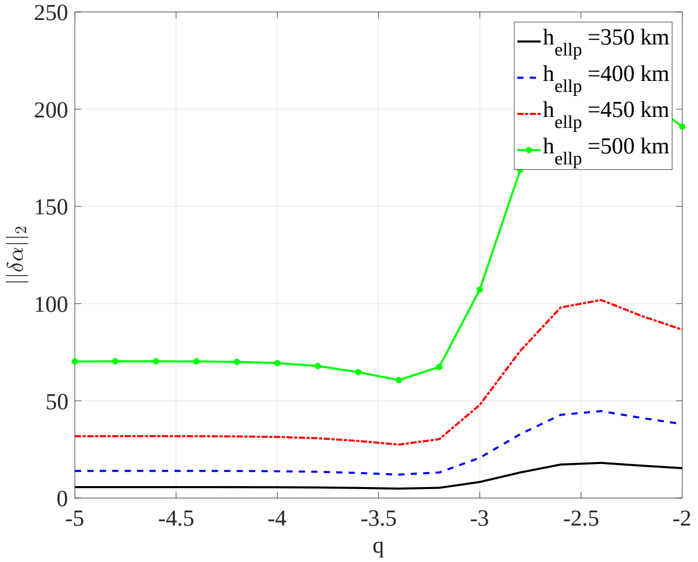

(b) $\delta\alpha$

Fig. 8: L_2-norm of PLQR control actions u_x and $\delta\alpha$ as a function of weighting factor q for (a) L_2-norm of u_x (b) L_2-norm of $\delta\alpha$

initial conditions of the leader and follower satellites with the control actions are propagated using HPOP, whereas the reference trajectories are propagated by using unperturbed two-body models. Then, the propagated inertial states are transformed to the RTN coordinate system to calculate the

Table 3: Reference numerical propagation force models

Force models	Geopotential	70×70 EGM-96
	Drag	Exponential model $C_D = 2.2$
	Third-Body	Solar/Lunar point masses based on Jet Propulsion Laboratory ephemerides, DE405
	Solar radiation	Conical shadow model, reflectivity factor $C_r = 1.2$
	Tidal effects	No tide forces.
Integrator	Runge Kutta 4^{th} order	
Time step	10 s	
Simulation period	Two days	

relative states between them [13, 30]. The proposed PLAE-based controller is used to generate u_x for implementation in the generation of thrust for the follower satellite and the estimation of $\delta\alpha$ to be used in the calculation of the areas of the leader and follower drag plates using the relations presented in Eq. (7).

Figure 10 illustrates the error components of the in-plane motion in the HPOP numerical simulation. The steady state of the error components for different altitudes are approximately equal to $0.1053, 0.0740, 0.0647$ and 0.0638 m in x-direction and $0.7703, 0.6826, 0.6446$ and 0.6442 m in y-direction, respectively. These represent errors less than 0.25% and 0.8% of the initial errors in x and y-directions. The controlled trajectories of the follower satellite are presented in Fig. 11. These results show that the parameterized output regulation algorithm is robust against all the perturbations that have not been modeled in HPOP for different altitudes. The control actions are presented in Fig. 12, which shows that the control input is already saturated in the transient region for altitudes $h_{ellp} \geq 350$ km, in which the stability is not guaranteed by the PLAE approach. The limits for the controller gains using the PLAE approach are highly restricted in comparison with the numerical simulations. Although, according to PLAE approach, the weighing factor ε^* should be lower than 10^{-8} for all the altitudes $h_{ellp} \geq 350$ km, as presented in Fig. 5, it is increased to $\varepsilon \leq 10^{-2}$ by using numerical simulations. This is because the stability margins are estimated

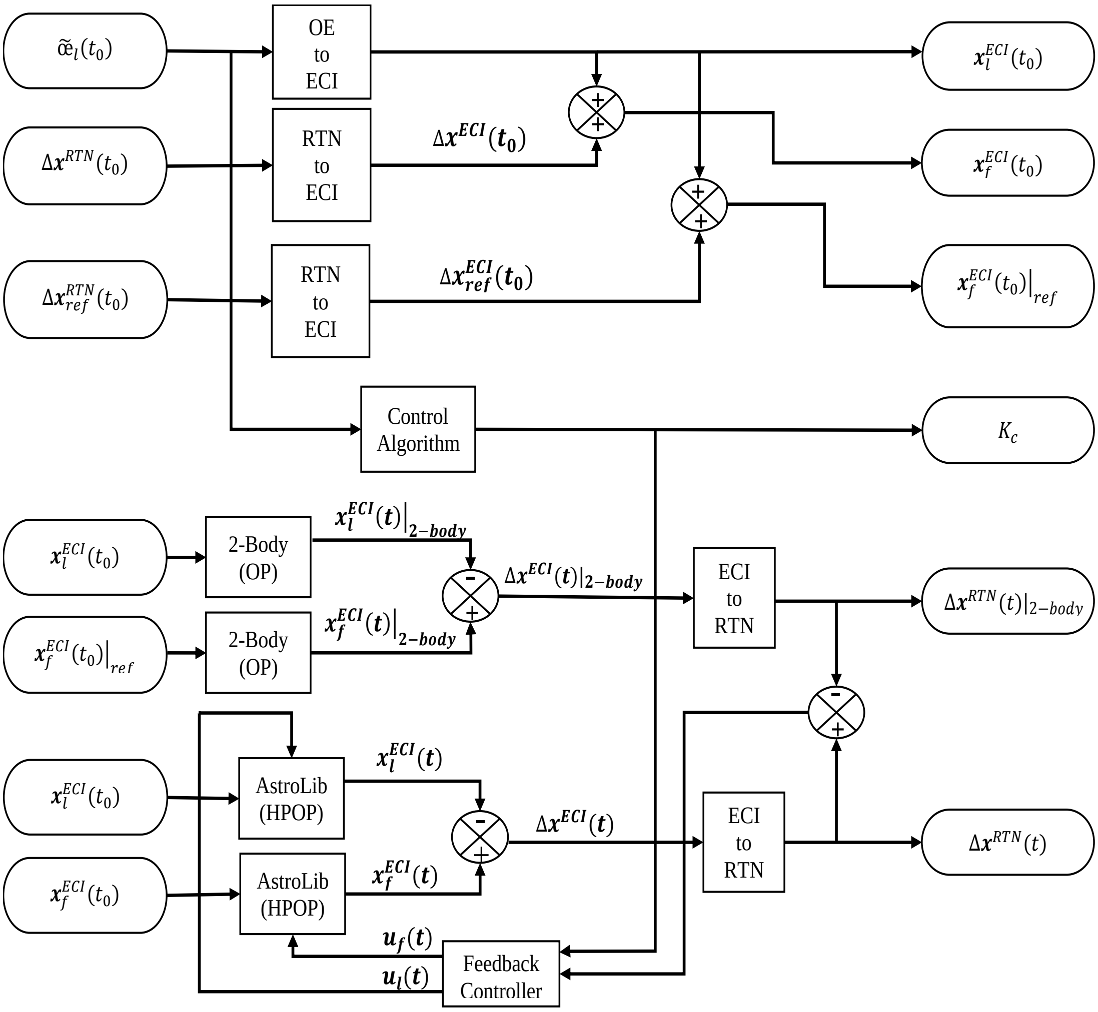

Fig. 9: Procedure for HPOP simulation.

based on the L_∞ norm of the error signal when using the PLAE approach.

The numerical simulations do not take the assumptions of equal and scalar V_{rel} for the leader and follower satellites into consideration. Any control algorithm based on these assumptions with extreme low gains would not be robust to handle errors for different $\boldsymbol{V_{rel}}$ vectors in more realistic models of the SS and HPOP numerical simulation. Furthermore, the need to address the uncertainties in the aerodynamic drag models [24, 33] also adversely affects the results for low-gain feedback systems. These errors may be handled by using an integral controller with the output regulation algorithm or by developing an adaptive output regulation control algorithm [40].

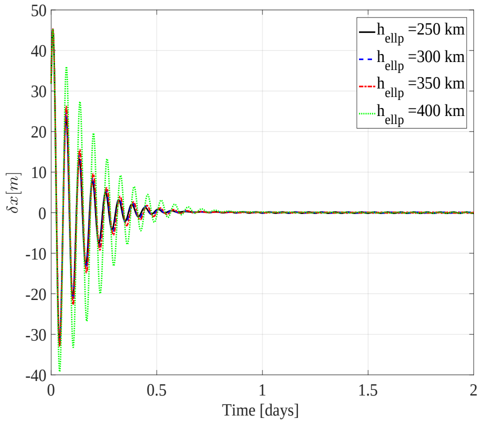

(a) x-component

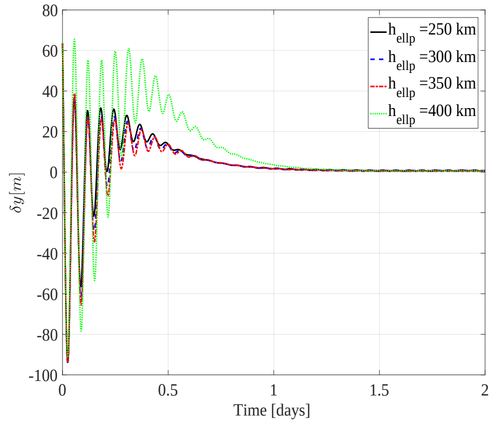

(b) y-component

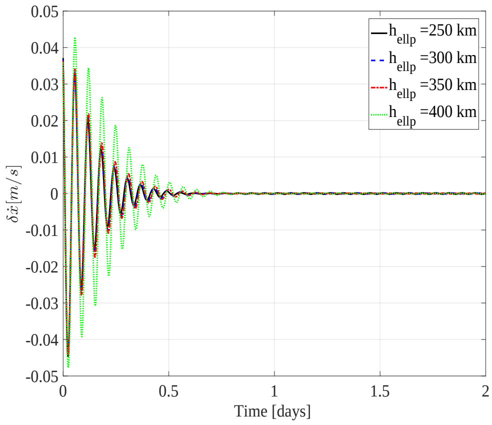

(c) $\dot{x}$-component

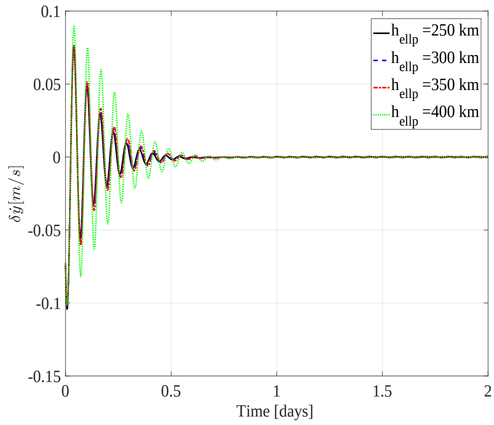

(d) $\dot{y}$-component

Fig. 10: HPOP error components for altitudes $h_{ellp} = 250, 300, 350, 400$ km

VI. Conclusion

This paper presented a practical approach to precisely control formation flying missions using a hybrid control action of thrust and differentials in aerodynamic drag. The control algorithm for the Sedwick-Schweighart perturbed linearized model was derived based on the parameterized output regulation theory. The low conservative PLAE approach was designed to approve the stability of the output regulation control system. The approach was developed to solve the output regulation problem subject to input saturation with different saturation limits using the parametric Lyapunov algebraic equation. Moreover, the region in which the parameter of the parametric Lyapunov algebraic equation remains stable can be determined for all formation flying missions.

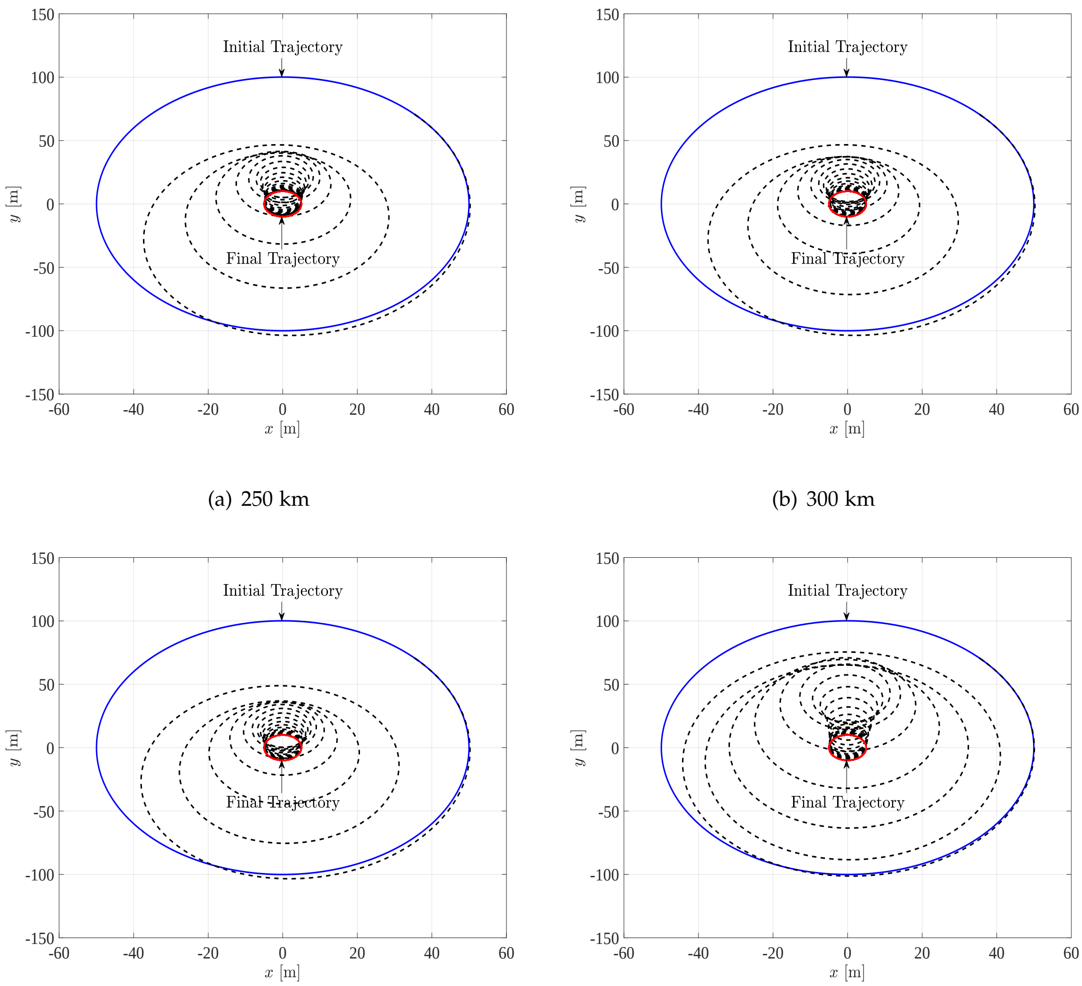

(a) 250 km

(b) 300 km

(c) 350 km

(d) 400 km

Fig. 11: HPOP in-plane formation flying controlled trajectories for altitudes

$$h_{ellp} = 250, 300, 350, 400 \text{ km}$$

The performance of the control algorithm was validated by using the high precision orbit propagator. The results obtained with the controlled numerical simulator models show that control action consisting of a combination of aerodynamic drag and thrust can track different reference trajectories with accurate steady-state errors of the order of centimeters. In the future work, we plan to concern ourselves with the inclusion of integration gains in the output regulation algorithm or the development of an adaptive output regulation algorithm to eliminate the need for the assumption of small formation radius and dealing with the uncertainties in the parameters such as atmospheric density and drag coefficient.

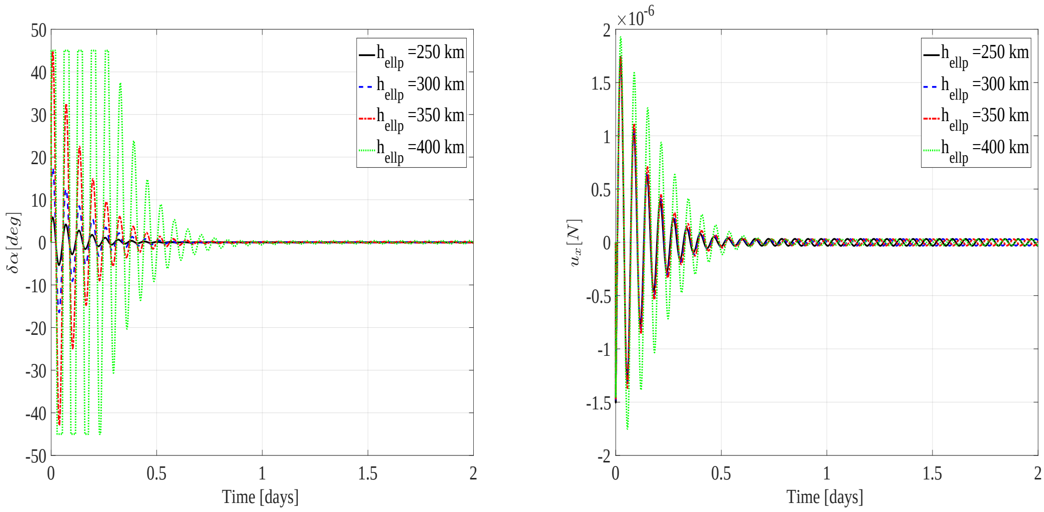

(a) $\delta\hat{\alpha}_d$ control action

(b) u_x control action

Fig. 12: HPOP control actions

VII. Acknowledgement

The authors thank Prof. Toshiya Hanada and the Space Systems and Dynamics Laboratory of Kyushu University for their support in implementing the orbit propagator software (AstroLib) for the verification process. The authors are also thankful for help received from Eng. Ahmed Ismail in the Space Division, National Authority for Remote Sensing and Space Sciences, Egypt for testing the performance of the control algorithm using his custom-built high-precision orbit propagator in the early stages of the verification process.

VIII. Appendix

A. Derivation of PLAE

Assume that the algebraic Riccati equation (ARE)

$$A^T P_\varepsilon + P_\varepsilon A - P_\varepsilon B_2 R^{-1} B_2^T P_\varepsilon + Q_\varepsilon = 0 \tag{34}$$

with $Q_\varepsilon = \varepsilon P_\varepsilon$. Then

$$A^T P_\varepsilon + P_\varepsilon A - P_\varepsilon B_2 R^{-1} B_2^T P_\varepsilon + \varepsilon P_\varepsilon = 0 \tag{35}$$

$$\Leftrightarrow P_\varepsilon^{-1} A^T + A P_\varepsilon^{-1} - B_2 R^{-1} B_2^T + P_\varepsilon^{-1} \varepsilon = 0 \tag{36}$$

$$\Leftrightarrow W_\varepsilon A^T + A W_\varepsilon - B_2 R^{-1} B_2^T + W_\varepsilon \varepsilon = 0 \tag{37}$$

$$\Leftrightarrow W_\varepsilon A_\varepsilon^T + A_\varepsilon W_\varepsilon - B_2 R^{-1} B_2^T = 0 \tag{38}$$

where $W_\varepsilon = P_\varepsilon^{-1}$ and $A_\varepsilon = A + \frac{1}{2}\varepsilon I_n$. This equation can be transformed to $A_\varepsilon^{*T} W_\varepsilon + W_\varepsilon A_\varepsilon^* + C_1^T C_1 = 0$ that presents the PLAE where $A_\varepsilon^* = -A^T - \frac{1}{2}\varepsilon I_n$ and $C_1 = R^{-1/2} B_2^T$. Therefore if $W_\varepsilon = P_\varepsilon^{-1}$ is the positive definite solution to the PLAE, P_ε is the positive definite solution for the ARE (34) and $\lim_{\varepsilon \to 0} P_\varepsilon = 0$. This proves that Q_ε is positive definite $\forall \varepsilon > 0$. It can also be confirmed that $\frac{dQ_\varepsilon}{d\varepsilon} = P_\varepsilon + \varepsilon \frac{dP_\varepsilon}{d\varepsilon} > 0$, as $(A_\varepsilon^T \frac{dP_\varepsilon}{d\varepsilon} + \frac{dP_\varepsilon}{d\varepsilon} A_\varepsilon) = -P_\varepsilon$, while A_ε is Hurwitz for $Q_\varepsilon = \varepsilon P_\varepsilon$ and P_ε is positive definite, so $\frac{dP_\varepsilon}{d\varepsilon} > 0$ and consequently $\frac{dQ_\varepsilon}{d\varepsilon} > 0$.

References

[1] A. N. Balaji Shankar Kumar, K. Yoshihara, Flight dynamics and control of the jc2sat mission, in: AAS/AIAA Astrodynamics specialist conference, Mackinac Island, 2007, Paper –AAS 07-410.

[2] B. S. Kumar, A. Ng, K. Yoshihara, A. D. Ruiter, Differential drag as a means of spacecraft formation control, in: Proceedings of the 2007 IEEE Aerospace Conference, Big Sky, MT, 2007, Paper –AAS 07-410. doi:10.1109/AERO.2007.352790.

[3] C. Sabol, R. Burns, C. A. McLaughlin, Satellite formation flying design and evolution, Journal of Spacecraft and Rockets 38 (2) (2001) 270–278. doi:10.2514/2.3681.

[4] W. H. Clohessy, R. S. Wiltshire, Terminal guidance system for satellite rendezvous, Journal of the aerospace sciences 27 (9) (1960) 653–658. doi:10.2514/8.8704.

[5] G. W. Hill, Researches in the lunar theory, American Journal of Mathematics 1 (1) (1878) 5–26.

[6] R. Sedwick, D. Miller, E. Kong, Mitigation of differential perturbations in clusters of formation flying satellites, in: 9th, Annual space flight mechanics: Spaceflight mechanics, Breckenridge, 1999, Paper –AAS 99-124.

[7] S. Schweighart, R. Sedwick, A perturbative analysis of geopotential disturbances for satellite formation flying, in: Proceedings of the IEEE Aerospace Conference, NJ, 2001, Paper –AAS 99-124. doi:10.1109/AERO.2001.931281.

[8] S. Schweighart, R. Sedwick, High-fidelity linearized j2 model for satellite formation flight, Journal of Guidance, Control, and Dynamics 25 (6) (2002) 1073–1080. doi:10.2514/2.4986.

[9] K. Yamanaka, F. Ankersen, New state transition matrix for relative motion on an arbitrary elliptical orbit, Journal of Guidance, Control, and Dynamics 25 (1) (2002) 60–66. doi:10.2514/2.4875.

[10] R. A. Broucke, Solution of the elliptic rendezvous problem with the time as independent variable, Journal of Guidance, Control, and Dynamics 26 (4) (2003) 615–621. doi:10.2514/2.5089.

[11] D.-W. Gim, K. T. Alfriend, State transition matrix of relative motion for the perturbed noncircular reference orbit, Journal of Guidance, Control, and Dynamics 26 (6) (2003) 956–971. doi:10.2514/2.6924.

[12] A. W. Koenig, T. Guffanti, S. D'Amico, New state transition matrices for relative motion of spacecraft formations in perturbed orbits, in: AAS/AIAA Astrodynamics specialist conference (AIAA 2016-5635), 2016. doi:10.2514/6.2016-5635.

[13] J. Sullivan, S. Grimberg, S. D'Amico, Comprehensive survey and assessment of spacecraft relative motion dynamics models, Journal of Guidance, Control, and Dynamics 40 (8) (2017) 1837–1859. doi:10.2514/1.G002309.

[14] S. Schweighart, R. Sedwick, Cross-track motion of satellite formations in the presence of j2 disturbances, Journal of Guidance, Control, and Dynamics 28 (5) (2005) 824–826. doi:10.2514/1.12387.

[15] C. L. Leonard, W. M. Hollister, E. V. Bergmann, Orbital formation-keeping with differential drag, Journal of Guidance, Control, and Dynamics 12 (1) (1989) 108–113. doi:10.2514/3.20374.

[16] H. Wong, V. Kapila, A. Sparks, Adaptive output feedback tracking control of multiple spacecraft, in: Proceedings of the American Control Conference, Arlington, VA, 2001. doi:10.1002/rnc.679.

[17] H. Jigang, Z. Yulin, Application of phase-plane method in the co-plane formation maintenance of formation flying satellites, in: Proceedings of the 25th Chinese Control Conference, Harbin, Heilongjiang, 2006.

[18] R. Bevilacqua, J. S. Hall, M. Romano, Multiple spacecraft rendezvous maneuvers by differential drag and low thrust engines, Celestial Mechanics and Dynamical Astronomy 106 (1) (2010) 69–88. doi:10.1007/s10569-009-9240-3.

[19] K. D.Kumar, A. K.Misra, S. Varma, T. Reid, F. Bellefeuille, Maintenance of satellite formations using environmental forces, ActaAstronautica 102 (2014) 341–354. doi:10.1016/j.actaastro.2014.05.001.

[20] T. Reid, A. K.Misra, Formation flight of satellites in the presence of atmospheric drag, Journal of Aerospace Engineering, Sciences and Applications 3 (1) (2011) 64–91. doi:10.7446/jaesa.0301.05.

[21] S. Varma, K. D. Kumar, Multiple satellite formation flying using differential drag, Journal of Spacecraft and Rockets 49 (2) (2012) 325–336. doi:10.2514/1.52395.

[22] M. Pastorelli, R. Bevilacqua, S. Pastorelli, Differential-drag-based roto-translational control for propellant-less spacecraft, ActaAstronautica 114 (2015) 6–21. doi:10.1016/j.actaastro.2015.04.014.

[23] H. Cho, L. Dell'Elce, G. Kerschen, Chattering-free sliding mode control for propellantless rendezvous using differential drag, in: 6th International Conference on Astrodynamics Tools and Techniques (ICATT), Darmstadt, Germany, 2016, Paper –AAS 07-410.
URL http://hdl.handle.net/2268/205641

[24] L. Mazal, D. Perez, R. Bevilacqua, Spacecraft rendezvous by differential drag under uncertainties, Journal of Guidance, Control, and Dynamics 39 (8) (2016) 1721–1733. doi:10.2514/1.G001785.

[25] M. Shouman, A. M. Atallah, Control of high fidelity linearized model for satellite formation flight using aerodynamic drag, in: AAS/AIAA Astrodynamics specialist conference, Napa, California, 2016, Paper –AAS 16-347.

[26] Z. Lin, A. Saberi, Semi-global exponential stabilization of linear systems subject to input saturation via linear feedbacks, Systems and Control Letters 21 (3) (1993) 225—239. doi:10.1109/ACC.1994.735152.

[27] A. Saberi, A. A. Stoorvogel, P. Sannuti, Control of linear systems with regulation and input constraints, 1st Edition, Springer-Verlag London, London, UK, 2000, Ch. 3, pp. 69–119.

[28] B. Zhou, Z. Lin, G.-R. Duan, Lyapunov differential equation approach to elliptical orbital rendezvous with constrained controls, Journal of Guidance, Control, and Dynamics 34 (2) (2011) 345–358. doi:10.2514/1.52372.

[29] D. A.Vallado, Fundamentals of astrodynamics and applications, 4th Edition, Microcosm Press, Inc, Hawthorne, CA, USA, 2013, Ch. 3,6, pp. 145–174,388–411.

[30] H. Schaub, J. L. Junkins, Analytical mechanics of space systems, 3rd Edition, AIAA Education Series, AIAA, Reston, VA,, USA, 2003, Ch. 14, pp. 709–768.

[31] B. B. Hajovsky, Satellite formation control using atmospheric drag, Ph.D. thesis, Department of Aeronautics and Astronautics, Graduate School of Engineering and Management,Air Force Institute of Technology, USA (2007).

[32] K. T. Alfriend, H. Schaub, D.-W. Gim, Gravitational pertubations,nonlinearity and circular orbit assumption effects on formation flying control strategies, in: AAS Guidance and Control Conference, Breckenridge, CO, 2000, Paper –AAS 00-012.

[33] D. A.Vallado, D. Finkleman, A critical assessment of satellite drag and atmospheric density modeling, ActaAstronautica 95 (2014) 141–165. doi:10.2514/6.2008-6442.

[34] D. Perez, R. Bevilacqua, Differential drag-based reference trajectories for spacecraft relative maneuvering using density forecast, Journal of Spacecraft and Rockets 53 (1) (2016) 234–239. doi:10.2514/1.A33332.

[35] B. A. Francis, The linear multivariable regulator problem, SIAM J. Control and Optimization. 15 (3) (1977) 486–505. doi:10.1137/0315033.

[36] Z. Lin, A. A. Stoorvogel, A. Saberi, Output regulation for linear systems subject to input saturation, Automatica 32 (1) (1996) 29–47. doi:10.1109/CDC.1994.411463.

[37] M. Bando, A. Ichikawa, Active formation flying along an elliptic orbit, Journal of Guidance, Control, and Dynamics 36 (1) (2013) 324–332. doi:10.2514/1.57703.

[38] A. Graham, Kronecker products and matrix calculus: with applications, 1st Edition, ELLIS HORWOOD LIMITED, Market Cross House, Cooper Street, Chichester, West Sussex, PO19 lEB, England, 1981, Ch. 3, pp. 37–51.

[39] T. Hanada, T. Yasaka, Orbital evolution of cloud particles from explosions of geosynchronous objects, Journal of Spacecraft and Rockets 42 (6) (2005) 1070–1076. doi:10.2514/1.11998.

[40] M. Bando, A. Ichikawa, Adaptive output regulation of nonlinear systems described by multiple linear models, in: Proc. 9th IFACWorkshop Adaptation Learn. Control Signal Process, Vol. 9, Imperial Anichkov Palace, Russia, 2007, pp. 269–274. doi:10.3182/20070829-3-RU-4911.00044.